



# Dichotomy of magnetic effect between Weyl fermions and anomalous Hall effect in PrAlSi



Hongtao Rong<sup>1,2,11</sup>, Ao Zhang<sup>3,11</sup>, Fu Yu<sup>4,11</sup>, Meng Lyu<sup>1,5,6,11</sup>, Hang Li<sup>7</sup>, Masashi Arita<sup>8</sup>, Zhanyang Hao<sup>3</sup>, Qi Jiang<sup>9</sup>, Zhengtai Liu<sup>9</sup>, Mao Ye<sup>9</sup>, Yuxuan Guo<sup>6,10</sup>, Jingfeng Xu<sup>6,10</sup>, Chen Liu<sup>10</sup>, Jiaou Wang<sup>10</sup>, Shu Guo<sup>3</sup>, Le Wang<sup>3</sup>, Junhao Lin<sup>3</sup>, Kenya Shimada<sup>8</sup>, Enke Liu<sup>1,5,6</sup>✉, Junbao He<sup>4</sup>✉, Qihang Liu<sup>3</sup>✉ & Chaoyu Chen<sup>1,3</sup>✉

Three key aspects of magnetic topological materials, *i.e.*, band topology, magnetic order and anomalous transport are closely related with each other, laying the ground for exotic phenomena such as topological magnetoelectric and magneto-optical effects. Here in the ferromagnetic Weyl semimetal PrAlSi, we report negligible effect of magnetic order on the band structure featuring Weyl fermions, as directly observed by angle-resolved photoemission spectroscopy. Instead, both anomalous and normal Hall effects show clear temperature/magnetism dependence. While the longitudinal conductivity ( $\sigma_{xx}$ ) is deep in the empirically intrinsic region, the anomalous Hall conductivity ( $\sigma_{AHE}$ ) is quadratically proportional to  $\sigma_{xx}$ , suggesting giant anomalous Hall angle at moderate  $\sigma_{xx}$ . Our findings point to disentangled band topology and anomalous transport, as well as the possibility to achieve high  $\sigma_{AHE}$  in highly conductive, ultrathin PrAlSi, suitable for anomalous Hall sensors and spin-transfer torque application.

The interplay of band topology and magnetism in magnetic topological states of matter gives rise to novel transport phenomena such as anomalous Hall and Nernst effects<sup>1–3</sup>. These three key aspects are usually entangled with each other. For example, intrinsic magnetic topological insulator Mn-Bi-Te family has shown a cascade of properties reflecting such entanglement, including the gapped/gapless surface state Dirac cone<sup>4–7</sup>, Chern insulator/axion insulator states<sup>8,9</sup>, quantum anomalous Hall effect<sup>10</sup> and layer Hall effect<sup>11</sup>. In particular, ubiquitous (nearly) gapless surface Dirac cones in antiferromagnetic Mn-Bi-Te cast doubts on the effectiveness of surface magnetic moments, despite the long-range bulk magnetic order, a major puzzle remaining in this area<sup>12</sup>. Disentangling the interplay between topological band feature, magnetic order, and topological transport effect composes a critical task in this area.

Recently, a family of intrinsic magnetic topological materials, the Weyl semimetals RAlX (R = Ce, Pr, Nd, Sm; X = Si, Ge) emerge, exhibiting rich magnetic structures and physics. Crystallizing in a noncentrosymmetric space group  $I4_1/md$  (No. 109) ( $I4_1/amd$  (No. 141) in some cases<sup>13</sup>), RAlX hosts low-energy Weyl fermions in its paramagnetic band structure as a result of inversion symmetry breaking. Theoretically, long-range magnetic orders further split the Weyl pairs and induce more Weyl nodes<sup>14</sup>. Experimentally, Weyl nodes and Fermi arcs<sup>15–19</sup>, anomalous Hall/Nernst effect<sup>20–23</sup>, singular magnetoresistance<sup>24</sup> and tunable magnetic domains<sup>25</sup> have been

reported within this family. Furthermore, the Weyl nodes are in turn proposed to mediate exchange coupling and induce exotic magnetic texture<sup>26,27</sup>, suggesting strong entanglement between magnetism, band topology and transport effect. However, there are also results showing negligible effect of the magnetic order on the band structure<sup>28</sup> and the dependence<sup>18,22,23,29–31</sup> or independence<sup>32,33</sup> of anomalous Hall transport on the intrinsic band topology. These conflicting results call for a synergetic investigation of the magnetic effect on the topological band features and transport behavior.

In this work, we systematically study the evolution of band structure and transport behavior of PrAlSi with temperature crossing the ferromagnetic transition. Using angle-resolved photoemission spectroscopy (ARPES), we reveal termination dependent band features and especially multiple Weyl nodes, which agree with the existing reports and are captured by our density functional theory (DFT) calculations. However, these band features show no observable change with temperature crossing the ferromagnetic transition, suggesting decoupled band structure and magnetic order. In stark contrast, the anomalous and normal Hall effects both show clear temperature evolution, with the former only present in the ferromagnetic phase. The normal Hall conductivity ( $\sigma_{xy}^N$ ) shows nonlinear dependence with magnetic field and is described by a two-band model approach. The anomalous Hall conductivity ( $\sigma_{AHE}$ ) reaches as high as 4200  $\Omega^{-1}cm^{-1}$ , far exceeding the intrinsic Berry curvature contribution.

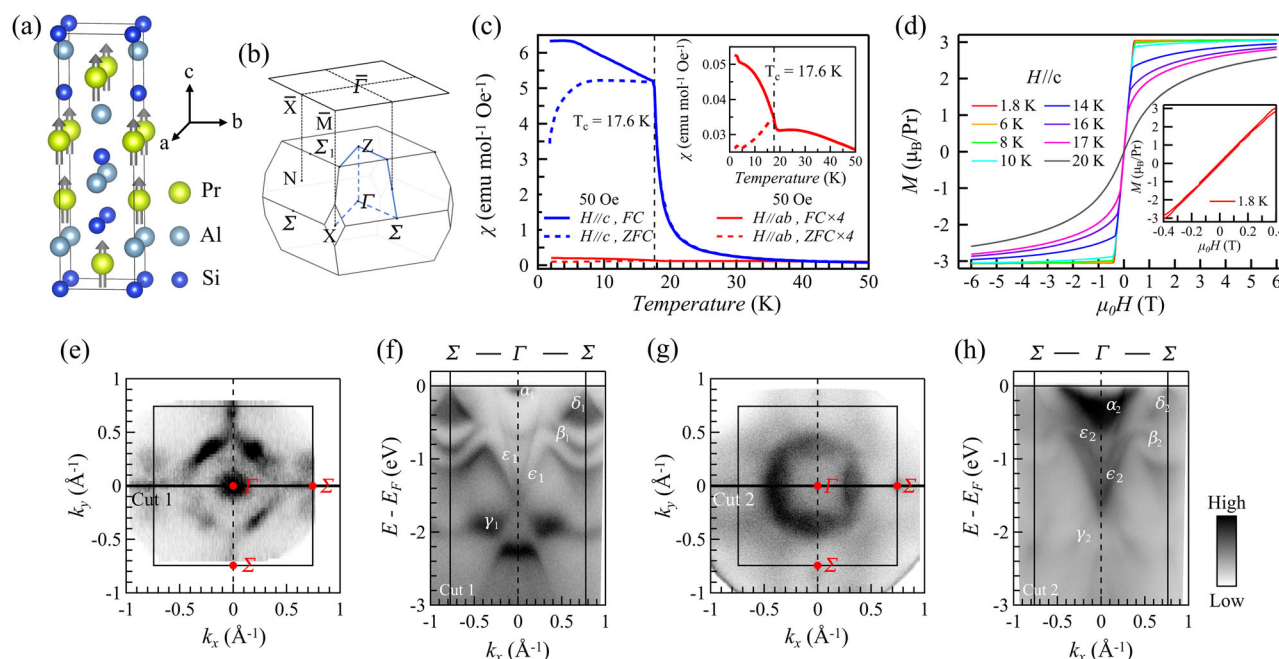


**Fig. 1 | Ferromagnetism and termination dependent band spectra of PrAlSi.** **a** Schematic crystal structure and magnetic structure of PrAlSi. **b** Sketches of three-dimensional Brillouin zone (BZ) and (001) surface BZ of PrAlSi. **c** Zero-field-cooled (ZFC) and field-cooled (FC) magnetic susceptibilities ( $\chi$ ) vs temperature ( $T$ ) for magnetic field ( $H = 50$  Oe) parallel to the  $c$  axis (blue lines) and the  $ab$  plane (red lines). Inset: the enlarged part of  $\chi$  vs  $T$  for  $H \parallel ab$ . **d** The magnetization curves for

$H \parallel c$  under different temperatures. Inset: the enlarged part of magnetization at 1.8 K. **e, f** ARPES Fermi surface mapping (**e**) and band spectra on the first termination. **g, h** Same as (**e, f**) but on the second termination. All the ARPES results are measured at 12 K (ferromagnetic state) using a photon energy of 40 eV with linear horizontal polarization, corresponding to the  $k_z = 0$  plane (for  $k_z$  dispersion see Supplementary Fig. S1).

Interestingly, while the longitudinal conductivity  $\sigma_{xx}$  is in the intrinsic region ( $10^4 \Omega^{-1} \text{cm}^{-1}$ ), the anomalous Hall conductivity  $|\sigma_{AHE}|$  is dominated by the skew scattering mechanism and proportional to  $\sigma_{xx}^2$ , pointing to giant anomalous Hall angle at easily accessible  $\sigma_{xx}$ . Our findings reveal the disentanglement between nontrivial band topology and anomalous Hall transport in PrAlSi, and the possibility to pursue very high anomalous Hall conductivity extrinsically in its two-dimensional limit.

## Results

### Termination dependent electronic structure of PrAlSi

PrAlSi family is commonly found to crystallize in a tetragonal structure with the nonsymmorphic space group of  $I4_1/\text{md}$  (No. 109)<sup>28,32</sup>. As illustrated in Fig. 1a, Pr, Al and Si atoms all form individual square net layers in the  $ab$  plane and stack along the  $c$  axis. Such a structure could give rise to multiple possible  $ab$  terminations up cleavage, for example, with terminations composed of Pr, Al, or Si atoms. As shown in Fig. 1c, the magnetic susceptibility  $\chi - T$  curves exhibit a ferromagnetic transition with  $T_C = 17.6 \text{ K}$  as evidenced by the clear bifurcation between ZFC and FC curves for both  $H \parallel c$  and  $H \parallel ab$ . An easy axis along  $c$  and an Ising-type exchange interaction are suggested as susceptibility for  $H \parallel c$  is two orders of magnitude higher than that for  $H \parallel ab$ . Furthermore, the magnetization  $M - H$  curves show small hysteresis loop at  $T = 1.8 \text{ K}$  and saturate to  $\sim 3\mu_B/\text{Pr}$  for  $\mu_0 H > 0.4 \text{ T}$ . All these behaviors agree with previous reports and establish a ferromagnetic ground state with Pr moments all aligned parallel to the  $c$  axis<sup>32,33</sup>.

In line with the lattice structure, ARPES Fermi surface mapping indeed found two types of terminations with distinct band and Fermi surfaces. While the first type is dominated by a rhombic feature centered at  $\Gamma$ , along with an electron pocket at  $\Gamma$  and the two circular bands located on both sides of  $\Sigma$  points (Fig. 1e), only one large circular pocket at  $\Gamma$  is well resolved in the second type (Fig. 1g). The predominant feature from the first termination (Fig. 1f) is an “X”-shaped, cone-like manifold at the BZ center, with the crossing located  $\sim 1.6 \text{ eV}$  below the Fermi level. In this termination, the spectral weight is stronger on the lower part of the “X”-shaped structure, particularly for  $\gamma_1$  band. The upper cone mainly

consists of sharp band  $\varepsilon_1$  and the broader band  $\epsilon_1$ . This dispersion also features an electron-like pocket  $\alpha_1$  near the Fermi level at  $\Gamma$  and  $\beta_1$  band which extends to about  $0.7 \text{ eV}$  below the Fermi level at the BZ center. Additionally, the BZ boundary is occupied by a hole band  $\delta_1$  with surface band merging into the bulk when approaching the Fermi level. For the second termination (Fig. 1h), the band dispersion also exhibits an “X”-shaped, cone-like feature. However, in contrast the first case, the spectral weight of the lower part of the “X”-shaped structure is noticeably weaker, especially for  $\gamma_2$  band. The upper cone also primarily consists of the sharp band  $\varepsilon_2$  and the broader band  $\epsilon_2$ . In this termination, an electron-like  $\alpha_2$  band at  $\Gamma$  appears larger and exhibits stronger spectral intensity compared to  $\alpha_1$  band.  $\beta_2$  band spans from BZ boundary to BZ center, reaching  $\sim 1.2 \text{ eV}$  below the Fermi level at  $\Gamma$ . In addition, the BZ boundary hole band  $\delta_2$  is hardly visible in the second termination. In the Supplementary Section II, we provide calculated the Fermi surfaces and band structures for different possible terminations. While some features are qualitatively consistent, a direct one-to-one correspondence between the theory and the experiment is not clearly established. A more comprehensive analysis would be needed to reliably identify the cleavage termination, which is beyond the current scope of this work.

### Absence of magnetic effect on Weyl fermions

The evolution of Weyl nodes in PrAlSi associated with the paramagnetic-ferromagnetic transition can be directly visualized from DFT calculations. For paramagnetic states (Fig. 2a, b), exactly on the  $k_z = 0$  plane, we find 8 Weyl nodes ( $W_1$ ) near the  $\Sigma$  points and 16 Weyl points ( $W_3$ ) close to the middle and on both sides of the  $\Gamma - X$  line. Beyond this plane, 16 Weyl nodes ( $W_2$ ) exist in the middle of the  $\bar{\Gamma} - \bar{\Sigma}$  line. In total there exist 40 Weyl points connecting the valence and conduction bands. For ferromagnetic state, magnetic moments align along the  $c$  axis, resulting in the breaking of  $C_{2z}T$  symmetry. As shown in Fig. 2c, d, this symmetry breaking causes a shift of  $W_1$  and  $W_3$  Weyl nodes along the  $k_z$  axis, no longer confined to the  $k_z = 0$  plane. The  $W_2$  Weyl nodes, previously existing as  $\pm k_z$  pairs, lose the symmetric distribution due to the symmetry breaking. In addition,

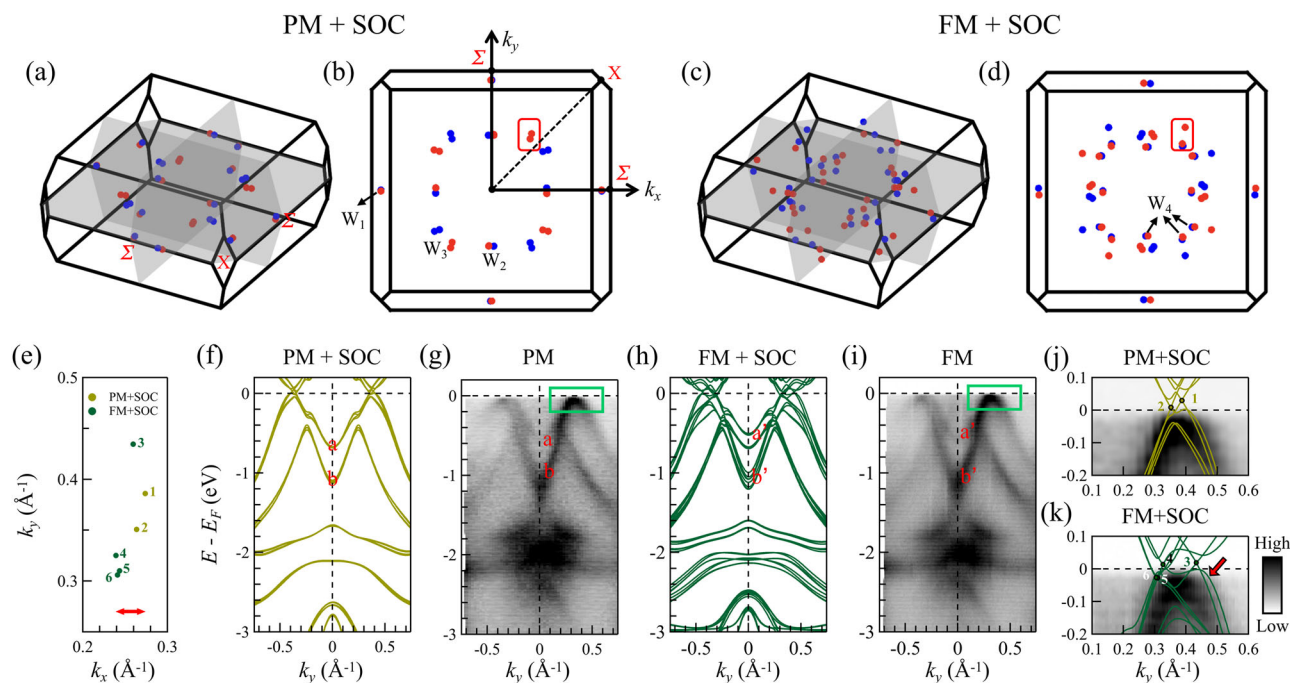


**Fig. 2 | Weyl fermions in paramagnetic and ferromagnetic states.** Configuration of the 40 Weyl nodes in paramagnetic state (PM) (a) and the 64 Weyl nodes in ferromagnetic (FM) state (c) in the bulk BZ with considering spin-orbital coupling (SOC). Projection of the Weyl nodes on the (001) surface BZ in PM state (b) and FM state (d). The blue (red) dots denote the Weyl node with chirality  $-1$  ( $+1$ ), respectively. e Sketch of the Weyl nodes in the red rectangle regions in panel (b) and (d). The DFT calculated band structures through Weyl node 1 and 2 along  $k_y$

direction in PM state (f) and through Weyl node 2–6 along  $k_y$  direction in FM state (h). The measured band spectra in the integrated momentum range from  $0.239 \text{ \AA}^{-1}$  to  $0.274 \text{ \AA}^{-1}$  at  $k_x$  direction in PM state (g) and FM state (i). The integrated range is shown by red, double headed arrow in panel e, j, k. Zoomed-in parts of the measured band spectra in the regions marked by the green rectangle in panel (g) and panel (i). Weyl nodes are marked by black circles in j and k. ARPES spectra shown here are measured using photon energy of 40 eV with linear horizontal polarization.

ferromagnetism leads to the emergence of 24 new Weyl nodes, designated as  $W_4$ . Thus, there are totally 64 Weyl nodes in ferromagnetic PrAlSi.

To enhance the visibility of the Weyl nodes on the (001) surface BZ, we magnify the areas within the red rectangle regions in Fig. 2b, d and show them collectively in Fig. 2e. In this figure, yellow points (1 and 2) depict Weyl nodes in the paramagnetic state, while dark green points (3, 4, 5 and 6) indicate those in ferromagnetic state. Figure 2f shows the DFT calculated band structures along  $k_y$  direction in the paramagnetic state, which are the superposition of dispersions cutting through Weyl nodes 1 and 2. Similarly, Fig. 2h presents the calculated ferromagnetic band structures containing dispersions cutting through Weyl nodes 3, 4, 5 and 6 (Supplementary Section III). The ARPES spectra corresponding to the paramagnetic (Fig. 2g) and ferromagnetic (Fig. 2i) states come from the integration along the  $k_x$  direction over a range covering all the 6 Weyl nodes. Satisfactory agreement between DFT calculation and ARPES spectral can be found, particularly for the dispersive features such as band  $a$  ( $a'$ ) and  $b$  ( $b'$ ). Note that, while ferromagnetism shifts Weyl nodes 3, 4, 5, 6 away from the  $k_z = 0$  plane, such  $k_z$  deviation is less than  $\sim 0.057 \text{ \AA}^{-1}$ , comparable to the intrinsic photoemission  $k_z$  broadening. Consequently, ARPES spectra corresponding to the  $k_z = 0$  plane shown here should contain contribution from all these 6 Weyl nodes.

To resolve any possible band spectral change associated to the magnetic order, we plot the zoom-in ARPES spectra and DFT calculation for both paramagnetic (Fig. 2j) and ferromagnetic (Fig. 2k) states. All the 6 Weyl nodes predicted by DFT are located very close to the Fermi level ( $\pm 30 \text{ meV}$ ). In particular, Weyl nodes 5 and 6 locate below the Fermi level, accessible in the ARPES spectra. While DFT predicted energy shift of the Weyl nodes and large band splitting in the ferromagnetic state, no such change can be resolved in the ARPES spectra. For example, Weyl nodes 3 and 4 in ferromagnetic state are expected by splitting or moving of the Weyl nodes in paramagnetic state. However, bands generated by Weyl node 3 and Weyl node 4 in ferromagnetic state (marked by the red arrow in Fig. 2(k)) are

absent in the ARPES spectra. These observations point to the negligible effect of ferromagnetic order on the band structure.

### Giant, extrinsic anomalous Hall conductivity

Many RAlX compounds show anomalous Hall effect arising from the intrinsic Berry curvature<sup>18,22,23,29–31</sup>, while the correlation with magnetism is not obvious<sup>34</sup>. Here we provide direct evidence that in PrAlSi, the anomalous Hall effect is dominated by extrinsic effect and relies on the ferromagnetic order. The longitudinal resistivity  $\rho_{xx}$  in Fig. 3a shows very low resistivity at the low temperature ( $\sim 15 \mu\Omega \text{ cm}$  at 2K), indicating high crystalline quality. The magnetoresistances (Fig. 3b) exhibit non-saturating behavior for magnetic field up to 9T. The measured Hall resistivities  $\rho_{yx}$  all exhibit positive slope (Fig. 3c), and a kink feature develops at low temperature for  $\sigma_{yx}$  (Fig. 3d) at the magnetic field which is coincident with the saturation field of the magnetization (Fig. 1d). This suggests that  $\sigma_{yx}$  should contain anomalous contribution  $\sigma_{yx}^A$  which is proportional to the magnetization. Consequently, Hall conductivity  $\sigma_{yx}$  is decomposed into anomalous Hall resistivity  $\sigma_{yx}^A$  (Fig. 3e) and normal Hall resistivity  $\sigma_{yx}^N$ , with the latter must being smooth at the saturation field. The corresponding anomalous Hall conductivity  $\sigma_{AHE} = \sigma_{yx}^A$  (Fig. 3e) and normal Hall conductivity  $\sigma_{xy}^N$  (Fig. 3gf) are then obtained for various temperatures. As shown in Fig. 3e,  $\sigma_{AHE}$  can reach  $\sim 4200 \Omega^{-1} \text{ cm}^{-1}$  at 2K. The normal part  $\sigma_{xy}^N$  is nonlinear to the magnetic field and can be well described by a two-band model (Fig. 3g) for the whole magnetic field range ( $-9\text{T}$  to  $9\text{T}$ ). The two-band model describes the normal Hall conductivity in terms of carrier concentrations ( $n_e$ ,  $n_h$ ) and Hall mobilities ( $\mu_e$ ,  $\mu_h$ ),  $\sigma_{xy}^N(B) = n_e e \mu_e^2 B / (1 + \mu_e^2 B^2) - n_h e \mu_h^2 B / (1 + \mu_h^2 B^2)$ . The fitting parameters are summarized in Fig. 3h–i, from which a clear temperature dependence can be resolved for both the carrier concentrations and Hall mobilities. Furthermore, the Hall resistivity also shows oscillation behavior at low temperature and high field regime (Fig. 3j–k), yielding one oscillation frequency of  $\sim 50\text{T}$  (Fig. 3l), in line with the previous report<sup>33</sup>. In general, the anomalous Hall effect only exists in the



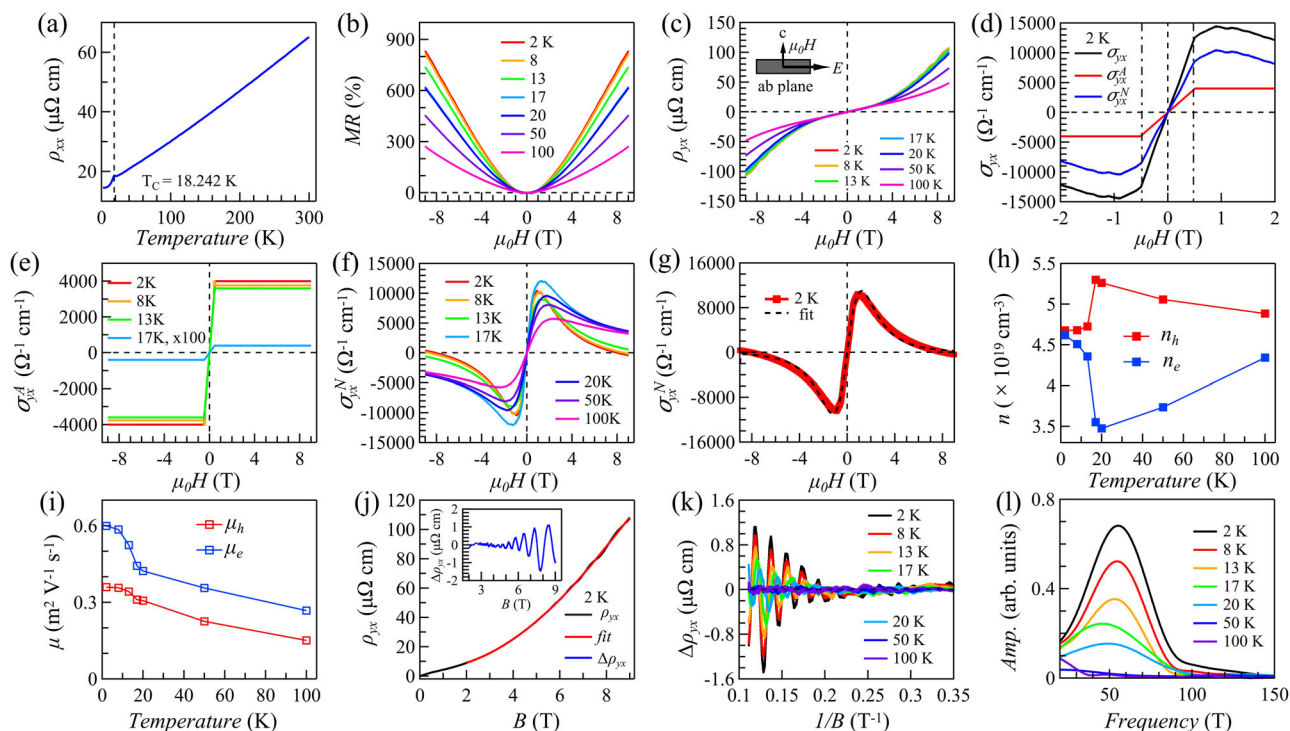


**Fig. 3 | The anomalous and normal Hall effect of PrAlSi.** **a** Longitudinal resistivity  $\rho_{xx}$  vs  $T$  in zero field. The magnetic field is applied along the  $c$  axis and the current along the  $ab$  plane (inset of **c**). **b** Magnetoresistances obtained in the temperature range from 2 K to 100 K. **c** Hall resistivities  $\rho_{yx}$  vs magnetic field under different temperatures. **d**  $\rho_{yx}$  at 2 K, which is decomposed into a normal part ( $\sigma_{yx}^N$ ) and an anomalous part ( $\sigma_{yx}^A$ ). **e** The decomposed  $\sigma_{yx}^A$  at various temperatures. **f** The decomposed normal Hall conductivities  $\sigma_{xy}^N$  under different temperatures. **g**  $\sigma_{xy}^N$  at

2 K (red line) and the fitting result by using a two-band model (black dashed line). **h, i** Carrier concentrations ( $n_e$  and  $n_h$ ) and mobilities ( $\mu_e$  and  $\mu_h$ ) under different temperature, from two-band fitting. **j** The representative Hall resistivity ( $\rho_{yx}$ ) taken at 2 K. Inset: the oscillatory part ( $\Delta\rho_{yx}$ ) of the Hall resistivity by subtracting a polynomial background. **k** Oscillation components ( $\Delta\rho_{yx}$ ) under different temperatures. **l** The Fast Fourier transform (FFT) spectra of  $\Delta\rho_{yx}$  oscillations at various temperatures.

ferromagnetic state and the normal Hall effect shows clear temperature dependence, suggesting strong correlation between the magnetism and transport phenomena.

To gain insight into the origin of the large anomalous Hall conductivity, we first calculate the intrinsic anomalous Hall conductivity  $\sigma_{yx}^A$  by integrating the Berry curvature over the occupied states. As shown in Fig. 4a, although  $\sigma_{yx}^A$  reaches about  $800 \Omega^{-1}\text{cm}^{-1}$  at 0.9 eV above the Fermi level, it is only about  $200 \Omega^{-1}\text{cm}^{-1}$  near the Fermi level, one order of magnitude lower than the value observed experimentally. This points to the extrinsic nature of the observed large  $\sigma_{yx}^A$ . To explore the possible microscopic mechanisms of the extrinsic  $\sigma_{yx}^A$ , the scaling relation  $\sigma_{yx}^A$  vs  $\sigma_{xx}$  among five PrAlSi samples is analyzed (Fig. 4b). According to the empirical model, intrinsic  $\sigma_{yx}^A$  is independent of  $\sigma_{xx}$ . In the region of high longitudinal conductivity,  $\sigma_{yx}^A$  is dominated by the skew scattering mechanism and proportional to  $\sigma_{xx}$  or  $\sigma_{xx}^2$ . Figure 4b, c display  $\sigma_{yx}^A$  versus  $\sigma_{xx}$  in double logarithmic scale. Although all the PrAlSi samples show longitudinal conductivity located deep in the intrinsic region with  $4 \times 10^4 < \sigma_{xx} < 8 \times 10^4 \Omega^{-1}\text{cm}^{-1}$ , the anomalous Hall conductivity clearly shows  $\sigma_{yx}^A \sim \sigma_{xx}^2$  behavior as highlighted by the blue dashed line in Fig. 4b, suggesting a predominant skew scattering mechanism. This mechanism arises from asymmetric scattering of spin-polarized electrons by impurities or defects in the presence of spin-orbit coupling. The probability of an electron scattering to the left or right depends on its spin orientation. In PrAlSi, the onset of ferromagnetism aligns the spins, enhancing this asymmetry and giving rise to a large anomalous Hall response. The fact that anomalous Hall effect only appears in the ferromagnetic phase further confirms the direct link between skew scattering and magnetic ordering.

Note that similar  $\sigma_{yx}^A \sim \sigma_{xx}^2$  behavior has been observed not only in traditional anomalous Hall materials such as Fe film<sup>35</sup>, but also in discovered V-based Kagome metals<sup>36</sup>. In PrAlSi, the quadratic dependence of  $\sigma_{yx}^A$  on  $\sigma_{xx}$  starts around  $4 \times 10^4 \Omega^{-1}\text{cm}^{-1}$ , one order of magnitude smaller than that in

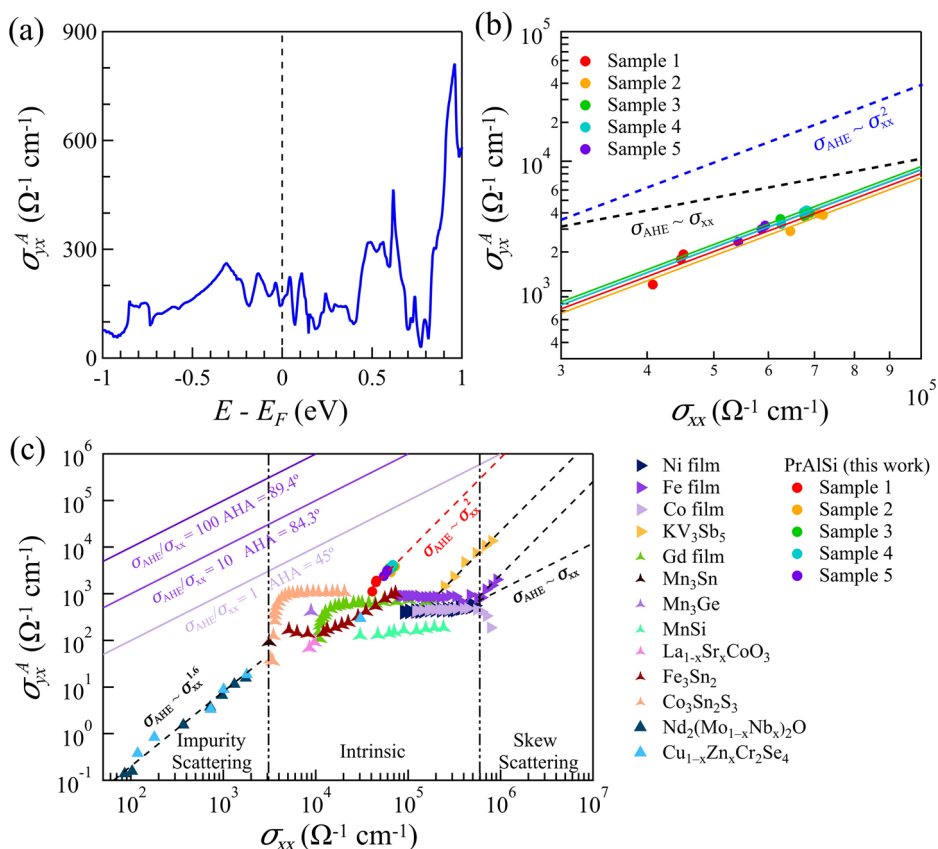
V-based Kagome metals<sup>36</sup> and nearly two orders of magnitude before Fe film<sup>35</sup>. This implies that high value of anomalous Hall ratio ( $\sigma_{AHE}/\sigma_{xx}$ ) and anomalous Hall angle ( $AHA = \tan^{-1}(\sigma_{AHE}/\sigma_{xx})$ ) can be achieved at moderate  $\sigma_{xx}$  in PrAlSi. As shown in Fig. 4c, the AHA of 45° can be expected at  $\sigma_{xx} \approx 2 \times 10^6 \Omega^{-1}\text{cm}^{-1}$ .

## Discussion

Combining synergetic ARPES, DFT and transport analyses, we have disentangled the correlation between long-range magnetic order, topological band features and anomalous Hall transport. Such conclusion is likely applicable to the whole RAlX family sharing a common crystal structure and band topology framework. From the available reports, for  $R = \text{Ce, Pr, Nd, Sm}$  and  $X = \text{Ge, Si}$ , temperature dependent transport experiments demonstrate close correspondence between the anomalous Hall effect and magnetization<sup>21–23,29–34,37</sup>. By contrast, while subtle band splitting by the ferromagnetic order is reported in CeAlSi<sup>38</sup>, no clear magnetic effect on the band structure and nontrivial band topology can be observed in most of the RAlX members. The negligible effect of the magnetic order on the band structure is reminiscent of the gapless topological surface states in antiferromagnetic topological insulator Mn-Bi-Te, providing another example of decoupling between long-range magnetic order and band topology. One natural explanation for this phenomenon is the weak effective coupling between conduction bands and Pr  $f$  orbitals contributing magnetism. According to a resonant photoemission study<sup>28</sup>, the Pr  $f$  states are mainly located 4 eV below the Fermi level, leading to the speculation of weak  $c-f$  hybridization. Another possibility is the complex spin structure deviating from ideal ferromagnetic order, either for the bulk<sup>33</sup> or just for the surface region, calling for further microscopic study on the surface magnetic order.

While the strong coupling between magnetism and band topology has been the only approach experimentally proved to realize the quantum anomalous Hall effect<sup>10,39</sup>, the decoupled magnetic order and band

**Fig. 4 | Extrinsic nature of the anomalous Hall effect.** **a** The calculated anomalous Hall conductivity. **b**, **c** Scaling relation of anomalous Hall effect for various materials. Panel **b** is the enlarged part of panel **c** and only displays the data of PrAlSi samples. The data of other materials were taken from references and therein<sup>40,51–59</sup> in panel **c**. Purple lines represent three anomalous Hall ratios ( $\sigma_{\text{AHE}}/\sigma_{\text{xx}}$ ) and their corresponding anomalous Hall angles ( $\text{AHA} = \tan^{-1}(\sigma_{\text{AHE}}/\sigma_{\text{xx}})$ ). The data of Sample 2 is shown in Fig. 3 and that of Sample 1, 3–5 is shown in Supplementary Section V.



topology seem discouraging. However, in Fig. 4c we point out one possibility that giant anomalous Hall angle can be achieved via increasing  $\sigma_{xx}$  to the orders of  $10^6 - 10^7 \Omega^{-1} \text{ cm}^{-1}$ . Indeed, several materials such as Fe and Gd films<sup>40</sup> have demonstrated the tunability of  $\sigma_{xx}$  in the range of one or two orders of magnitude. One could also expect such tunability in the ultrathin films of PrAlSi with optimized crystalline quality. Such extrapolation suggests extremely high anomalous Hall conductivity can be achieved in highly conductive, ultrathin PrAlSi films, holding great potential in applications such as anomalous Hall sensors<sup>41</sup> and those based on spin-transfer torque<sup>42</sup>.

## Methods

### Sample growth and characterization

Single crystals of PrAlSi were grown by flux method. The stoichiometry of starting raw materials of Pr, Si and Al is 1 : 1 : 10 in molar ratio. The mixture was put into an alumina crucible and sealed in a quartz tube. The quartz tube was heated slowly to 1050 °C, held for 20h, and then cooled to 700 °C at a rate of 2 °C/h, where the flux was decanted using a centrifuge. Finally, the residual flux was removed by dissolving in the sodium hydroxide solution. The obtained single crystals are in the form of plate-like crystals with a typical dimension of  $10 \times 10 \times 1 \text{ mm}^3$ . Magnetic measurements were performed using the QD Magnetic Property Measurement System (MPMS) with the Vibrating Sample Magnetometer (VSM) mode.

### Transport measurements

The electrical transport was measured in a Quantum Design PPMS-9T. To measure the electrical transport, the single crystals were cut into a rectangle with dimensions of  $1.5 \times 0.5 \times 0.1 \text{ mm}^3$  and a standard six-probe method was applied. To eliminate the influence of the voltage probe misalignment, the longitudinal ( $\rho_{xx}$ ) and transverse ( $\rho_{yx}$ ) resistivities were measured for both positive and negative fields ( $\rho_{xx}(\mu_0 H) = (\rho_{xx}(+\mu_0 H) + \rho_{xx}(-\mu_0 H))/2$  and  $\rho_{yx}(\mu_0 H) = (\rho_{yx}(+\mu_0 H) - \rho_{yx}(-\mu_0 H))/2$ ).

### ARPES measurements

ARPES measurements were performed at the beamline BL03U of the Shanghai Synchrotron Radiation Facility (SSRF), the beamline 9 A of the Hiroshima Synchrotron Radiation Center (HSRC), and the beamline 4B9B of Beijing Synchrotron Radiation Facility (BSRF). The energy and angular resolutions were set at 10 meV and  $0.1^\circ$ . Samples were cleaved in-situ along the (001) crystal plane in an ultrahigh vacuum better than  $5 \times 10^{-11} \text{ mbar}$ .

### First-principles calculations

The first-principles calculations utilized projector-augmented-wave (PAW) method<sup>43</sup>, within the Vienna ab initio simulation package (VASP)<sup>44</sup>. The exchange and correlation effects were accounted by the generalized gradient approximation (GGA) using the Perdew-Burke-Ernzerhof (PBE) formalism<sup>45</sup>. An energy cut off of 273 eV was employed for the calculations. The whole Brillouin-zone was sampled by  $12 \times 12 \times 6$  Monkhorst-Pack grid<sup>46</sup> for all cells. Due to the local magnetic moments contributed by *f* electrons in Pr atoms, the GGA + U approach<sup>47</sup> within the Dudarev scheme<sup>48</sup> was applied, with the U value for Pr atom set at 4 eV. The maximally localized Wannier function was constructed using the WANNIER90 package<sup>49</sup> and the WannierTools package<sup>50</sup> was utilized to calculate the surface states and the position of Weyl points.

### Data availability

The experimental data and calculated data that support the findings of this work are available from the corresponding author upon reasonable request.

### Code availability

The codes for analysing the data of this study are available from the corresponding authors upon reasonable request.

Received: 17 July 2024; Accepted: 28 April 2025;

Published online: 05 May 2025

## References

- Hasan, M. Z. et al. Weyl, Dirac and high-fold chiral fermions in topological quantum matter. *Nat. Rev. Mater.* **6**, 784–803 (2021).
- Bernevig, B. A., Felser, C. & Beidenkopf, H. Progress and prospects in magnetic topological materials. *Nature* **603**, 41–51 (2022).
- Wang, Y. et al. Intrinsic magnetic topological materials. *Front. Phys.* **18**, 21304 (2023).
- Hao, Y.-J. et al. Gapless surface dirac cone in antiferromagnetic topological insulator MnBi<sub>2</sub>Te<sub>4</sub>. *Phys. Rev. X* **9**, 041038 (2019).
- Ma, X.-M. et al. Hybridization-induced gapped and gapless states on the surface of magnetic topological insulators. *Phys. Rev. B* **102**, 245136 (2020).
- Wu, X. et al. Distinct topological surface states on the two terminations of MnBi<sub>4</sub>Te<sub>7</sub>. *Phys. Rev. X* **10**, 031013 (2020).
- Lu, R. et al. Half-magnetic topological insulator with magnetization-induced dirac gap at a selected surface. *Phys. Rev. X* **11**, 011039 (2021).
- Liu, C. et al. Robust axion insulator and Chern insulator phases in a two-dimensional antiferromagnetic topological insulator. *Nat. Mater.* **19**, 522–527 (2020).
- Ge, J. et al. High-Chern-number and high-temperature quantum Hall effect without Landau levels. *Natl. Sci. Rev.* **7**, 1280–1287 (2020).
- Deng, Y. et al. Quantum anomalous Hall effect in intrinsic magnetic topological insulator MnBi<sub>2</sub>Te<sub>4</sub>. *Science* **367**, 895–900 (2020).
- Gao, A. et al. Layer Hall effect in a 2D topological axion antiferromagnet. *Nature* **595**, 521–525 (2021).
- Wang, Y. et al. On the topological surface states of the intrinsic magnetic topological insulator Mn-Bi-Te family. *Natl. Sci. Rev.* **11**, nwad066 (2023).
- Puphal, P. et al. Bulk single-crystal growth of the theoretically predicted magnetic Weyl semimetals RAlGe (R = Pr, Ce). *Phys. Rev. Mater.* **3**, <https://doi.org/10.1103/PhysRevMaterials.3.024204> (2019).
- Chang, G. et al. Magnetic and noncentrosymmetric Weyl fermion semimetals in the RAlGe family of compounds (R=rare earth). *Phys. Rev. B* **97**, <https://doi.org/10.1103/PhysRevB.97.041104> (2018).
- Sakhya, A. P. et al. Observation of Fermi arcs and Weyl nodes in a noncentrosymmetric magnetic Weyl semimetal. *Phys. Rev. Mater.* **7**, <https://doi.org/10.1103/PhysRevMaterials.7.L051202> (2023).
- Xu, S.-Y. et al. Discovery of Lorentz-violating type II Weyl fermions in LaAlGe. *Sci. Adv.* **3**, e1603266 (2017).
- Li, C. et al. Emergence of Weyl fermions by ferrimagnetism in a noncentrosymmetric magnetic Weyl semimetal. *Nat. Commun.* **14**, 7185 (2023).
- Sanchez, D. S. et al. Observation of Weyl fermions in a magnetic non-centrosymmetric crystal. *Nat. Commun.* **11**, 3356 (2020).
- Zhang, Y. et al. Kramers nodal lines and Weyl fermions in SmAlSi. *Commun. Phys.* **6**, 134 (2023).
- Piva M. M. et al. Topological features in the ferromagnetic Weyl semimetal CeAlSi: Role of domain walls. *Phys. Rev. Res.* **5**, <https://doi.org/10.1103/PhysRevResearch.5.013068> (2023).
- Yang, H.-Y. et al. Noncollinear ferromagnetic Weyl semimetal with anisotropic anomalous Hall effect. *Phys. Rev. B* **103**, 115143 (2021).
- Destraz, D. et al. Magnetism and anomalous transport in the Weyl semimetal PrAlGe: possible route to axial gauge fields. *NPJ Quantum Mater.* **5**, 5 (2020).
- Meng, B. et al. Large anomalous Hall effect in ferromagnetic Weyl semimetal candidate PrAlGe. *APL Mater.* **7**, <https://doi.org/10.1063/1.5090795> (2019).
- Suzuki, T. et al. Singular angular magnetoresistance in a magnetic nodal semimetal. *Science* **365**, 377–381 (2019).
- Sun Y. et al. Mapping domain-wall topology in the magnetic Weyl semimetal CeAlSi. *Phys. Rev. B* **104**, <https://doi.org/10.1103/PhysRevB.104.235119> (2021).
- Yao, X. et al. Large topological hall effect and spiral magnetic order in the weyl semimetal SmAlSi. *Phys. Rev. X* **13**, <https://doi.org/10.1103/PhysRevX.13.011035> (2023).
- Gaudet, J. et al. Weyl-mediated helical magnetism in NdAlSi. *Nat. Mater.* **20**, 1650–1656 (2021).
- Lou, R. et al. Signature of weakly coupled f electrons and conduction electrons in magnetic Weyl semimetal candidates PrAlSi and SmAlSi. *Phys. Rev. B* **107**, <https://doi.org/10.1103/PhysRevB.107.035158> (2023).
- Alam, Md. S. et al. Sign change of anomalous Hall effect and anomalous Nernst effect in the Weyl semimetal CeAlSi. *Phys. Rev. B* **107**, 085102 (2023).
- Cho, K. et al. Large anomalous Hall effect and intrinsic Berry curvature in magnetic Weyl semimetal NdAlGe. *Mater. Today Commun.* **35**, <https://doi.org/10.1016/j.mtcomm.2023.106411> (2023).
- Dhital, C. et al. Multi-k magnetic structure and large anomalous Hall effect in candidate magnetic Weyl semimetal NdAlGe. *Phys. Rev. B* **107**, 224414 (2023).
- Yang, H.-Y. et al. Transition from intrinsic to extrinsic anomalous Hall effect in the ferromagnetic Weyl semimetal PrAlGe<sub>1-x</sub>Si<sub>x</sub>. *APL Mater.* **8**, <https://doi.org/10.1063/1.5132958> (2020).
- Lyu, M. et al. Nonsaturating magnetoresistance, anomalous Hall effect, and magnetic quantum oscillations in the ferromagnetic semimetal PrAlSi. *Phys. Rev. B* **102**, <https://doi.org/10.1103/PhysRevB.102.085143> (2020).
- Yang, H.-Y. et al. Stripe helical magnetism and two regimes of anomalous Hall effect in NdAlGe. *Phys. Rev. Mater.* **7**, 034202 (2023).
- Tian, Y., Ye, L. & Jin, X. Proper scaling of the anomalous Hall effect. *Phys. Rev. Lett.* **103**, 087206 (2009).
- Yang, S.-Y. et al. Giant, unconventional anomalous Hall effect in the metallic frustrated magnet candidate, KV<sub>3</sub>Sb<sub>5</sub>. *Sci. Adv.* **6**, eabb6003 (2020).
- Gao, Y. et al. Anomalous Hall effect emerging from field-induced Weyl nodes in SmAlSi. *arXiv:2310.09364* (2023).
- Cheng, E. et al. Tunable positions of Weyl nodes via magnetism and pressure in the ferromagnetic Weyl semimetal CeAlSi. *Nat. Commun.* **15**, 1467 (2024).
- Chang, C.-Z. et al. Experimental observation of the quantum anomalous hall effect in a magnetic topological insulator. *Science* **340**, 167 (2013).
- Miyasato, T. et al. Crossover behavior of the anomalous Hall effect and anomalous nernst effect in itinerant ferromagnets. *Phys. Rev. Lett.* **99**, 086602 (2007).
- Zhang, Y., Hao, Q. & Xiao, G. Low-frequency noise of magnetic sensors based on the anomalous hall effect in Fe–Pt alloys. *Sensors* **19**, <https://doi.org/10.3390/s19163537> (2019).
- Iihama, S. et al. Spin-transfer torque induced by the spin anomalous Hall effect. *Nat. Electron.* **1**, 120–123 (2018).
- Kresse, G. & Joubert, D. From ultrasoft pseudopotentials to the projector augmented-wave method. *Phys. Rev. B* **59**, 1758–1775 (1999).
- Kresse, G. & Furthmüller, J. Efficient iterative schemes for ab initio total-energy calculations using a plane-wave basis set. *Phys. Rev. B* **54**, 11169–11186 (1996).
- Perdew, J. P., Burke, K. & Ernzerhof, M. Generalized gradient approximation made simple. *Phys. Rev. Lett.* **78**, 1396–1396 (1997).
- Monkhorst, H. J. & Pack, J. D. Special points for Brillouin-zone integrations. *Phys. Rev. B* **13**, 5188–5192 (1976).
- Lichtenstein, A. I., Anisimov, V. I. & Zaanen, J. Density-functional theory and strong interactions: Orbital ordering in Mott-Hubbard insulators. *Phys. Rev. B* **52**, R5467–R5470 (1995).
- Dudarev, S. L., Botton, G. A., Savrasov, S. Y., Humphreys, C. J. & Sutton, A. P. Electron-energy-loss spectra and the structural stability of nickel oxide: An LSDA+U study. *Phys. Rev. B* **57**, 1505–1509 (1998).
- Mostofi, A. A. et al. wannier90: A tool for obtaining maximally-localised Wannier functions. *Comput. Phys. Commun.* **178**, 685–699 (2008).



50. Wu, Q., Zhang, S., Song, H.-F., Troyer, M. & Soluyanov, A. A. WannierTools: An open-source software package for novel topological materials. *Comput. Phys. Commun.* **224**, 405–416 (2018).
51. Onoda, S., Sugimoto, N. & Nagaosa, N. Intrinsic versus extrinsic anomalous Hall effect in ferromagnets. *Phys. Rev. Lett.* **97**, 126602 (2006).
52. Iguchi, S., Hanasaki, N. & Tokura, Y. Scaling of anomalous hall resistivity in Nd<sub>2</sub>(Mo(1-x)Nb(x))<sub>2</sub>O<sub>7</sub> with spin chirality. *Phys. Rev. Lett.* **99**, 077202 (2007).
53. Miyasato, T. et al. Anomalous Hall effect and Nernst effect in itinerant ferromagnets. *J. Magn. Magn. Mater.* **310**, 1053–1055 (2007).
54. Onoda, S., Sugimoto, N. & Nagaosa, N. Quantum transport theory of anomalous electric, thermoelectric, and thermal Hall effects in ferromagnets. *Phys. Rev. B* **77**, <https://doi.org/10.1103/PhysRevB.77.165103> (2008).
55. Nakatsuji, S., Kiyohara, N. & Higo, T. Large anomalous Hall effect in a non-collinear antiferromagnet at room temperature. *Nature* **527**, 212–215 (2015).
56. Nayak, A. K. et al. Large anomalous Hall effect driven by a nonvanishing Berry curvature in the noncollinear antiferromagnet Mn<sub>3</sub>Ge. *Sci. Adv.* **2**, e1501870 (2016).
57. Liu, E. et al. Giant anomalous Hall effect in a ferromagnetic Kagome-lattice semimetal. *Nat. Phys.* **14**, 1125–1131 (2018).
58. Ye, L. et al. Massive Dirac fermions in a ferromagnetic kagome metal. *Nature* **555**, 638–642 (2018).
59. Yang, S. Y. et al. Giant, unconventional anomalous Hall effect in the metallic frustrated magnet candidate, KV(3)Sb(5). *Sci. Adv.* **6**, eabb6003 (2020).

## Acknowledgements

This work is supported by Guangdong Basic and Applied Basic Research Foundation (Grants No.2021B1515130007, 2022B1515130005 and 2022B1515020046), the National Key R&D Program of China (Grants No.2022YFA1403700 and 2022YFB3608000), the National Natural Science Foundation of China (NSFC)(Grants No.12074163), the Guangdong Innovative and Entrepreneurial Research Team Program (Grant No.2019ZT08C044), Shenzhen Science and Technology Program (Grant No. RCJC20221008092722009 and No. 20231117091158001), the Innovative Team of General Higher Educational Institutes in Guangdong Province (Grant No. 2020KCXTD001). Synchrotron ARPES measurements were conducted at multiple facilities. Part of this research was carried out at beamline 9 A of the Hiroshima Synchrotron Radiation Center (HSRC), with the approval of the Proposal Assessing Committee (Proposals No. 22BG011, 22BG024, 23BG017 and 23BG018).

## Author contributions

H.T.R. and C.Y.C. proposed and designed the research. Y.F. and J.B.H. contributed to sample growth. H.T.R., M.L., H.L. and E.K.L. contributed to

transport measurement. S.G., L.W. and J.H.L. contributed to sample characterization. M.A. and K.S. contributed to the development and maintenance of the beamline 9 A at Hiroshima Synchrotron Radiation Center (HSRC). Q.J., Z.T.L. and M.Y. contributed to the development and maintenance of BL03U at Shanghai Synchrotron Radiation Facility (SSRF). Y.X.G., J.F.X., C.L. and J.O.W. contributed to the development and maintenance of the beamline 4B9B of Beijing Synchrotron Radiation Facility (BSRF). H.T.R., Z.Y.H. and C.Y.C. carried out the ARPES experiments. A.Z. and Q.H.L. performed the DFT calculations.

## Competing interests

The authors declare no competing interests.

## Additional information

**Supplementary information** The online version contains supplementary material available at <https://doi.org/10.1038/s43246-025-00816-0>.

**Correspondence** and requests for materials should be addressed to Enke Liu, Junbao He, Qihang Liu or Chaoyu Chen.

**Peer review information** *Communications Materials* thanks Zhaoming Tian and the other, anonymous, reviewer(s) for their contribution to the peer review of this work. Primary Handling Editors: Xiaokang Li and Aldo Isidori.

**Reprints and permissions information** is available at <http://www.nature.com/reprints>

**Publisher's note** Springer Nature remains neutral with regard to jurisdictional claims in published maps and institutional affiliations.

**Open Access** This article is licensed under a Creative Commons Attribution 4.0 International License, which permits use, sharing, adaptation, distribution and reproduction in any medium or format, as long as you give appropriate credit to the original author(s) and the source, provide a link to the Creative Commons licence, and indicate if changes were made. The images or other third party material in this article are included in the article's Creative Commons licence, unless indicated otherwise in a credit line to the material. If material is not included in the article's Creative Commons licence and your intended use is not permitted by statutory regulation or exceeds the permitted use, you will need to obtain permission directly from the copyright holder. To view a copy of this licence, visit <http://creativecommons.org/licenses/by/4.0/>.

© The Author(s) 2025

<sup>1</sup>Songshan Lake Materials Laboratory, Dongguan 523808, China. <sup>2</sup>Department of Physics, The Pennsylvania State University, University Park, PA 16802, USA.

<sup>3</sup>Department of Physics, State key laboratory of quantum functional materials, and Guangdong Basic Research Center of Excellence for Quantum Science, and Shenzhen Institute for Quantum Science and Engineering, Southern University of Science and Technology (SUSTech), Shenzhen 518055, China. <sup>4</sup>Henan International Joint Laboratory of MXene Materials Microstructure, College of Physics and Electronic Engineering, Nanyang Normal University, Nanyang 473061 Henan, China.

<sup>5</sup>Beijing National Laboratory for Condensed Matter Physics, Institute of Physics, Chinese Academy of Sciences, 100190 Beijing, China. <sup>6</sup>University of Chinese Academy of Sciences, 100049 Beijing, China. <sup>7</sup>Institute of Quantum Materials and Devices, School of Electronics and Information Engineering, Tiangong University, Tianjin 300387, China. <sup>8</sup>Research Institute for Synchrotron Radiation Science (HiSOR), International Institute for Sustainability with Knotted Chiral Meta Matter (WPI-SKCM2) and Research Institute for Semiconductor Engineering (RISE), Hiroshima University, Higashi-Hiroshima, Hiroshima, Japan. <sup>9</sup>Shanghai Synchrotron Radiation Facility, Shanghai Advanced Research Institute, Chinese Academy of Sciences, Shanghai 201204, China. <sup>10</sup>Beijing Synchrotron Radiation Facility, Institute of High Energy Physics, Chinese Academy of Sciences, 100049 Beijing, P. R. China. <sup>11</sup>These authors contributed equally: Hongtao Rong, Ao Zhang, Fu Yu, Meng Lyu. [ekliu@iphy.ac.cn](mailto:ekliu@iphy.ac.cn); [hejunbao@nynu.edu.cn](mailto:hejunbao@nynu.edu.cn); [liuqh@sustech.edu.cn](mailto:liuqh@sustech.edu.cn); [chenchaoyu@sslab.org.cn](mailto:chenchaoyu@sslab.org.cn)